Anisotropic shape of CsPbBr 3 colloidal nanocrystals: from 1D to 2D confinement effects

Violette Steinmetz, Julien Ramade, Laurent Legrand, Thierry Barisien, Frédérick Bernardot, Emmanuel Lhuillier, Mathieu Bernard, Maxime Vabre, Imen Saïdi, Amal Ghribi, et al.

▶ **To cite this version:**

Violette Steinmetz, Julien Ramade, Laurent Legrand, Thierry Barisien, Frédérick Bernardot, et al.. Anisotropic shape of CsPbBr 3 colloidal nanocrystals: from 1D to 2D confinement effects. Nanoscale, 2020, 10.1039/D0NR03901B . hal-02938698

HAL Id: hal-02938698

https://hal.sorbonne-universite.fr/hal-02938698v1

Submitted on 16 Sep 2020

HAL is a multi-disciplinary open access archive for the deposit and dissemination of scientific research documents, whether they are published or not. The documents may come from teaching and research institutions in France or abroad, or from public or private research centers.

L'archive ouverte pluridisciplinaire **HAL**, est destinée au dépôt et à la diffusion de documents scientifiques de niveau recherche, publiés ou non, émanant des établissements d'enseignement et de recherche français ou étrangers, des laboratoires publics ou privés.

ARTICLE

Anisotropic shape of $CsPbBr_3$ colloidal nanocrystals: from 1D to 2D confinement effects

Received 00th January 20xx,
Accepted 00th January 20xx

DOI: 10.1039/x0xx00000x

Violette Steinmetz, [a] Julien Ramade, [a] Laurent Legrand,*[a] Thierry Barisien, [a] Frédérick Bernardot, [a] Emmanuel Lhuillier, [a] Mathieu Bernard, [a] Maxime Vabre, [a] Imen Saïdi, [b] Amal Ghribi, [b] Kaïs Boujdaria, [b] Christophe Testelin [a] and Maria Chamarro [a]

We synthesized strongly anisotropic $CsPbBr_3$ nanocrystals with very narrow emission and absorption lines associated to confinement effects along one or two dimensions, called respectively nanoplatelets (NPLs) and nanosticks (NSTs). Transmission Electron Microscopy (TEM) images, absorption and photoluminescence (PL) spectra taken at low temperature are very precise tools to determine which kind of confinement has to be considered and to deduce the shape, the size and the thickness of nanocrystals under focus. We show that the energy of the band-edge absorption and PL peaks versus the inverse of the square of the NPL thickness has a linear behaviour from 11 monolayers (MLs) *ie* a thickness of 6.38 nm, until 4 MLs (2.32 nm) showing that self-energy correction compensates the increase of the exciton binding energy in thin NPLs as already observed in Cadmium chalcogenides-based NPLs. We also show that slight changes in the morphology of NSTs leads to a very drastic modification of their absorption spectra. Time-resolved PL of NSTs has a non-monotonous behaviour with temperature. At 5 K, a quasi-single exponential with a lifetime of 80 ps is obtained; at intermediate temperature, the decay is bi-exponential and at 150 K, a quasi-single exponential decay is recovered (≈ 0.4 ns). For NSTs, the exciton interaction with LO phonons governs the broadening of the absorption and PL peaks at room temperature and is stronger than in chalcogenides quantum dots and NPLs.

Introduction

Controlling the anisotropic growth of colloidal nanocrystals is a key issue in the generation of advanced materials with complex functionalities. Less than a decade ago, the anisotropy control in chalcogenide colloidal systems was demonstrated by obtaining nanorods[1] and structures with more complex geometries (like octapod-shaped nanocrystals[2]), or by the growth control along one direction in PbS;[3,4] ultimate monolayer level control was even shown in II-VI colloidal bidimensional nanocrystals.[5–10] The latter nanostructures called nanoplatelets (NPLs) retain the quantum confinement along one direction. They exhibit exceptional electronic properties, such as narrow emission lines at both cryogenic and room temperatures,[11] enhanced exciton binding energies[12,13] and absorption cross–section (scaling with the NPL area,[14] as well as low thresholds of two- and one-photon absorption pumped amplified emission and optical gain coefficient, 4-fold larger than in colloidal quantum dots.[15–17]

In the last five years, progresses in metal halide perovskite solar cells have fuelled research in these materials and renewed interest in nanostructured and colloidal materials. Multi-layered organic perovskite (like Ruddlesden–Popper halide perovskites) are natural 2D systems, with confinement effects along one direction.[18,19] In addition, several efforts have also been done to synthesize organic/inorganic NPLs[20–23] and nanowires,[22,24] or all-inorganic NPLs[25–31] as well as nanowires.[26,32,33] Long nanowires can be cut to obtain nano-objects with two confinement directions leading to nanorods or nanosticks (NSTs).[34] Several applications have also been proposed that could exploit such nanostructured perovskite materials, as for example, low-threshold lasers,[35–37] LEDs,[38,39] photodetectors[40,41] and flexible optoelectronic devices.[42] Size effects were mainly addressed in NPLs dispersed in solutions by measuring absorption or PL spectra at room temperature. There are much less studies in nanowires or NSTs[43] while there are experimental evidences that NSTs have better emissive properties than nanowires[34] and that they are systems where the size effects, in terms of quantum confinement, strongly depend on the shape.

[a] *Sorbonne Université, CNRS-UMR 7588, Institut des NanoSciences de Paris, INSP, 4 place Jussieu, F-75005, Paris, France. *E-mail: legrand@insp.jussieu.fr*
[b] *Université de Carthage, Faculté des Sciences de Bizerte, LR01ES15, Laboratoire de Physique des Matériaux : Structure et Propriétés, 7021, Zarzouna Bizerte, Tunisia.*

† Footnotes relating to the title and/or authors should appear here.
Electronic Supplementary Information (ESI) available: Chemicals synthesis of $CsPbBr_3$ nanocrystals, Spectroscopic data on nanosticks samples, Theoretical support. See DOI: 10.1039/x0xx00000x

Please do not adjust margins

In this work, we synthesized strongly anisotropic $CsPbBr_3$ nanocrystals exhibiting confinement effects in one or two dimensions associated to specific optical responses characterized by narrow emission and absorption lines. The synthesis methods used result in different nanocrystal geometries, depending on the post-growth (aged sample) or the in-growth conditions (addition or not of HBr). As far as the anisotropic shape is concerned two classes of systems are indeed obtained: in the following, we will distinguish nanocrystals characterized by a strong confinement, essentially along one direction (thickness) *ie* NPLs, from nanocrystals having their optical properties determined by an additional confinement length (lateral size) *ie* nanosticks (NSTs). Because room temperature spectroscopic data are broadened by electron- phonon interaction,[44] throughout this work, as a complement to TEM investigations, low temperature absorption and PL studies are privileged in order to precisely correlate spectroscopic features to the level of confinement and shape anisotropy in each of the structures. We demonstrate a large and accurate tunability of the absorption and the emission energies by the size and shape anisotropy control of $CsPbBr_3$ nanocrystals. A simple model that considers a strong confinement regime gives fundamental insights to understand the observed 1D- and 2D confinement effects. Finally, we particularly focus on the optical properties of NSTs, a new appealing class of colloidal nanocrystals.

Experimental methods

Two types of syntheses have been used, without (Synthesis A) or with (Synthesis B) addition of HBr (see ESI, section I.). The samples elaborated for spectroscopic measurements consisted of a spin-coated deposited or drop-casted dilute solution onto a glass slide. No difference in optical properties was observed depending on sample preparation.

For structural characterization through TEM, the prepared solution was diluted in hexane and a drop was deposited for impregnation on a copper grid coated by amorphous carbon. The TEM grids have been degased under secondary vacuum overnight to remove volatile solvent. TEM observations were performed with a JEOL-2010F operated at 200 kV.

Optical transmission spectra were recorded using a CARY 5000 double-beam spectrophotometer (Agilent Company) with 0.4 nm resolution. For temperature-dependent studies, a helium exchange gas cryostat was used. The temperature was monitored between ≈ 11 K and ambient temperature by Si diodes and controlled by heating of the gas.

PL experiments were carried out as a function of temperature using a confocal-like microscope. For this study, we used a frequency doubled picosecond Ti:Sapphire laser operating at 82 MHz and tuned in the range 370-410 nm. The average excitation powers are a few µW in a spot of diameter close to 1.5 µm. The excitation laser beam is focused using a microscope objective with NA = 0.6. The samples are mounted on the cold finger of a cryostat (Oxford Instruments) designed to compensate for thermal expansion and to maintain the spatial position of the spot as temperature is changed. The luminescence collected with the same objective is analyzed in an ACTON SP2760i Roper Scientific-Princeton Instruments spectrometer coupled to a nitrogen-cooled SPEC10 (RS-PI) CCD camera, with an overall spectral resolution of ≈ 50 µeV. The objective located outside the cryostat is attached to a three-axis piezo stage, allowing to finely scan the sample.

Time-resolved PL experiments were carried out using a streak camera, C5680 model from Hamamatsu incorporating a M5675 synchroscan unit, synchronized with the picosecond Ti:Sapphire laser.

Results and discussion

The optical absorption and PL of $CsPbBr_3$ NPLs or NSTs are governed by excitons, the electron-hole pairs bound by the Coulomb interaction. In bulk, the band-edge excitons are constituted by an upper valence band hole state ($J_h = 1/2$; $J_h^z = \pm 1/2$) and an electron state from the lowest split-off conduction band, $J_e = 1/2$; $J_e^z = \pm 1/2$.[45,46] The energy corresponding to the fundamental state of this bulk exciton state is written:

$$E_{exc}^{bulk} = E_g - E_X \qquad (1)$$

where E_g is the energy gap and E_X the exciton binding energy in bulk materials. In order to evaluate these two quantities, we have performed a 40-band kp model in cubic phase perovskite (see ESI, section III.). We obtain for bulk $CsPbBr_3$ E_g = 2.37 eV and E_X = 32 meV and the corresponding Bohr radius a_X = 3.2 nm. That leads to $E_{exc}^{bulk} \approx 2.34$ eV. The calculated E_X can be compared to the binding energy of 40 meV obtained in poorly confined 16 nm cuboid nanocrystals with optical properties similar to the bulk material.[47]

In NPLs, a confinement effect is present along one direction, denoted here *z*, when the thickness, L_z , is such that $L_z \leq a_X$. In order to evaluate the energy of the first exciton optical transition $E_{1Se-1Sh}$, different contributions should be considered: (i) The confinement energy of the 'split-off' electron state and the upper hole state, denoted as E_e^{1S} and E_h^{1S} respectively. In the framework of the effective mass approach and for an infinite quantum well along the thickness direction, this energy writes $E_{e,h}^{1S} = \hbar^2\pi^2/(2m_{e,h}L_z^2)$ with $m_{e,h}$ the effective mass of the electron or hole respectively (L_z is the NPL thickness, defined above); (ii) The self-energy effects due to interaction of electrons and holes with their own image charges across the interface between the NPL material and the surrounding medium (solution or ligands). This term of interaction is a repulsive term. Recent theoretical calculations show that it becomes important only for NPLs having less than 4 MLs,[48] (iii) The exciton binding energy, E_b, increases with respect to the bulk when the NPL thickness decreases. This increase has two different origins: the first one is due to a

Please do not adjust margins

confinement effect, as observed in epitaxial quantum wells, and the second one is due to the decrease of the global dielectric constant as L_z decreases due to the mismatch of the dielectric constants between the surrounding medium, mostly made of low dielectric constant material and the NPL. In epitaxial quantum wells, the binding energy increases because the overlap between the electron and hole wave-functions increases as size decreases. E_b varies from the bulk value, E_X, when $L_z > a_X$, to almost 2 E_X when $L_z \approx a_X$ and has a theoretical limit at 4 E_X for very narrow quantum wells.[49] Because the exciton wave-function penetrates the barrier material the limit 4 E_X is usually not reached.[50] In epitaxial quantum wells, the effect of dielectric mismatch can be neglected. In perovskite NPLs, Sapori *et al.*[48] have calculated that a significant decrease of the dielectric constant with respect to its bulk value occurs only for structures with less than 4 MLs. Therefore, we do not expect an increase of the binding energy related to dielectric confinement for NPLs with more than 4 MLs.

We then write the energy of $E_{1Se-1Sh}$ transition, neglecting self-energy term, as follows:

$$E_{e,h}^{1S} = E_g - E_b + E_e^{1S} + E_h^{1S} = E_g - E_b + \hbar^2\pi^2/2\mu(a\,n)^2 \quad (2)$$

where $\mu^{-1} = m_e^{-1} + m_h^{-1}$ with μ the reduced exciton mass, $L_z = a\ n$, and where a is the thickness of a single octahedral layer and n the number of octahedral layers or MLs.

Figure 1a shows a TEM image of an aged sample, A1 (see SI, Table 1), *ie* a dropcasted $CsPbBr_3$ NPLs film after four months at room temperature and air in the dark. Large cubic or rectangular NPLs coexist with less numerous, smaller and thinner NPLs. Almost all the NPLs are placed face down with respect to the substrate and a small number is staked face to face and stand on their sides. Thickness of the staked NPLs is ≈ 3 nm (5 MLs correspond to 2.9 nm). The optical absorption spectra of this sample obtained at 12 K and room temperature are shown in Figure 1b. First, we underline that the energy of the lowest transition shifts to the blue when the temperature increases; that is the common behaviour in perovskite materials. The blue shift observed here, 70 meV, is of the same order of magnitude as the observed shift in $CsPbBr_3$ cuboid nanocrystals.[47] Second, a higher resolution is obtained at low temperature. Room-temperature spectra are mainly broadened by electron-phonon interaction[44] making difficult to extract information when different sizes or shapes are involved. That is why, from now on, only the low temperature absorption and PL spectra will be considered to analyze the signatures of the confinement. The peak energies run from 2.32 eV, energy very close to the calculated bulk band-gap value, to 2.69 eV (Figure 1b). We have listed them (see SI, Table 2) and attributed consecutive integers n to the energy of the more intense peaks. The energies are then plotted as a function of $1/n^2$ while optimizing the linear fit. The curve in Figure 1c corresponds to the association of the 2.69 eV energy to n = 5; the solid line is a fit of the experimental data to the expression given in Equation (2). The fit shows a good agreement with the expected linear law and provides a constant value of $E_g - E_b$ = 2.31 eV consistent with the value given by kp calculations in bulk materials (see SI, section III.). We also extract a slope of 9.56 eV consistent with the calculated value of μ = 0.117 in free electron mass units (see SI) and, more critically, with the value of a = 0.58 nm for the monolayer thickness.[28,29] The linear adjustment in the basic model of Equation (2) also corroborates theoretical studies[48] predicting that, in perovskite NPLs and up to 4 MLs, one can neglect both the self-energy correction and the variation in the exciton binding strength. We also underline that exciton resonance energies are remarkably sensitive to the number of ML with jumps in $E_{1Se-1Sh}$ close or lager than 100 meV as Δn = 1 and $n \leq 7$.

Figure 2a shows TEM of NPLs films (samples B1) synthesized following Synthesis B described in section I. of SI and modified with respect to Synthesis A by the addition of 240 µL de HBr. We clearly observe the critical effect of the HBr treatment. Samples are made of nanocrystals that are exclusively NPLs having a rectangular shape and lateral dimensions on the order of several hundreds of nanometers. For sample B2 obtained by following also synthesis B, the absorption and PL spectra obtained at 12 K and 5 K respectively are represented in Figure 2b. Using the previous analysis to correlate energies and thickness, we can conclude that NPLs of 4 to 7 MLs (4.06 nm) are the most representative ones in the sample. The peak corresponding to 4 MLs NPLs clearly shows up in the absorption as well as weaker peak corresponding to the 5 MLs contribution. Conversely, the 6 and 7 MLs contributions are more visible in the PL spectrum. Complementary measurements are presented in Figure 2c with the absorption and PL spectra of an equivalent NPLs sample, B3 (T ≈ 40 K). We underline that absorption is dominated at low energy by a narrow and intense peak at 2.9 eV that matches well the energy predicted by Equation (2) for 4 MLs NPLs. In sample B2 the energy for peak associated to 4 MLs is slightly different, 2.86 eV but in the same range (see Figure 2b). The PL, meanwhile, is dominated by the emission of thicker NPLs present in the sample and in smaller quantity (since we are not able to observe their contribution in absorption spectra). The 4 to 8 MLs (4.64 nm) contributions are clearly visible in PL of sample B3 (see also the inset Figure 2c). We note that, despite the size dispersion in the sample, exploiting the thickness dependent optical response of NPLs and the narrow lines in PL and absorption spectra, it is possible to selectively address NPLs with a given size.

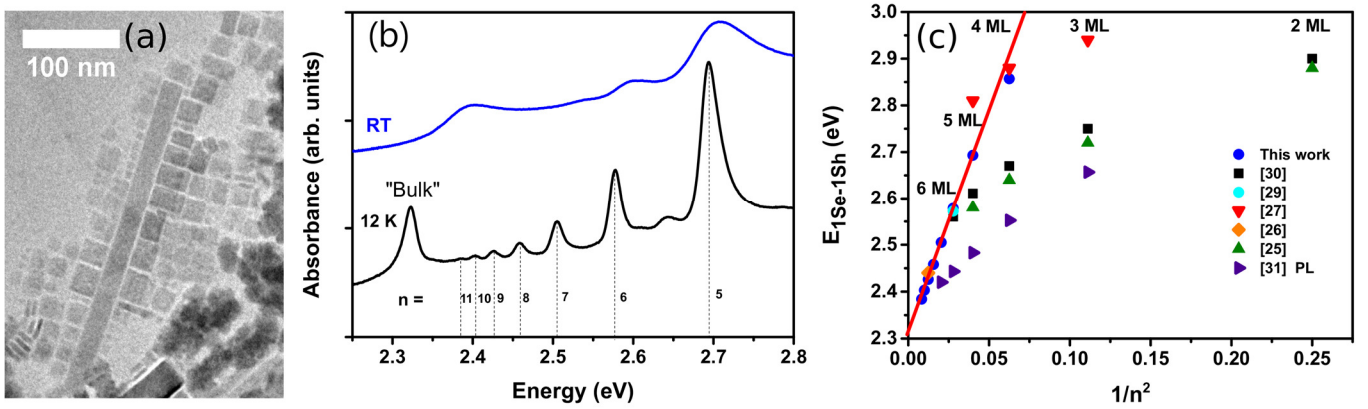

Figure 1: (a) Image of a self-organized NPLs film aged of a few months, sample A1. (b) Low temperature (12 K, black) and room temperature (blue) absorption spectra of a similar dropcasted $CsPbBr_3$ NPLs film after 4 months at ambiant temperature and air in the dark (sample A1). The number n from 5 to 11 close to the dotted lines marking absorption bands energies indicate the thicknesses L_z of NPLs in terms of interplanar distance a (L_z = n a). The concerned NPLs are assumed to be 2D systems (see text). (c) Energies of the absorption peaks numbered in (b) (blue full circles) as a function of $1/n^2$. From the linear fit (red line) to the absorption data shown in figure (b), the interplanar distance a ≈ 0.58 nm is obtained. Room-temperature absorption results from other groups are also represented. Note that reference [31] refers to photoluminescence results at 5 K.

In this work, the low temperature linewidths of the absorption peak corresponding to NPLs with 4 MLs typically range between 35 and 40 meV. We notice that the broadening is slightly reduced in NPLs with larger thicknesses and falls in the 18 - 25 meV interval. Obviously, these narrow linewidths, in particular at 2.86 - 2.9 eV, cannot be explained by fluctuations of 1-ML thickness that would lead to ~ 100 meV shifts of the transitions (see above), for the sub-set of NPLs probed by the light spot. We believe that the lateral dimension at a fixed thickness can differ from one NPL to another. A more comprehensive study of multiple confinement effects is brought below when considering NSTs. However, anticipating the results of the next section, we estimate that a decrease of the lateral dimension from tens of nm to 20 nm (10 nm) leads to a blue shifted absorption by ≈ 9 meV (30 meV). The influence of such residual inhomogeneities, while keeping moderate might thus play a role. We note that the intrinsic exciton fine structure modified by the strong confinement along the *z* direction can also contribute to the linewidth of the optical transitions. In cuboid nanocrystals with size smaller than Bohr diameter, an energy spread of band-edge exciton states of the order of several meV has been predicted.[45]

Finally, we compare our experimental results with data from other authors, focusing on absorption spectra instead of PL that is, in general, Stokes-shifted with respect to the absorption. The results are generally obtained in solution[51] and at room temperature. The fact that no cryogenic data are available in the literature is problematic as room temperature spectra are broadened by electron-phonon interaction[44] which is detrimental to the precise establishment of an energy size relationship.

Figure 1c summarizes also our results and those obtained by several authors.[26,27,29–31] First we underline that a very good agreement is found for 9 MLs (5.22 nm)[26] and for 6 MLs (3.48 nm).[29] However, the disagreement is important with data of reference 31 for almost all thickness values and these data are also very different from other data. We emphasize that the results of Bohn *et al*.[30] and Cho *et al*.[28] differ from ours only for NPL thinner than 5 MLs. Their experimental transition energies for NPLs with 4 and less MLs clearly deviate from the law given by Equation (2) which neglects the carriers self-energy, mainly, and the finite value of the confinement potential. Indeed, Sichert and coworkers[52] have demonstrated that the agreement between theory and experiment could be improved by considering a more realistic model for the confinement potential. Furthermore, when E_b is not constant and increases with decreasing NPL thickness, Equation (2) no more leads to a linear behaviour. Experimental studies have shown that the exciton binding energy of organic halide perovskite and II-VI NPLs with very few layers increases as the number of monolayers decreases.[13,19,53] Meanwhile, in II-VI NPLs the strengthening of the binding and the displacement induced by the self-interaction effects have shown comparable amplitudes so that Equation (2) satisfactorily governs the lowest exciton energy.[6,54] More studies would therefore be needed to understand the origin of differences in the size-dependent behaviour evidenced by the authors in thinner perovskite NPLs.

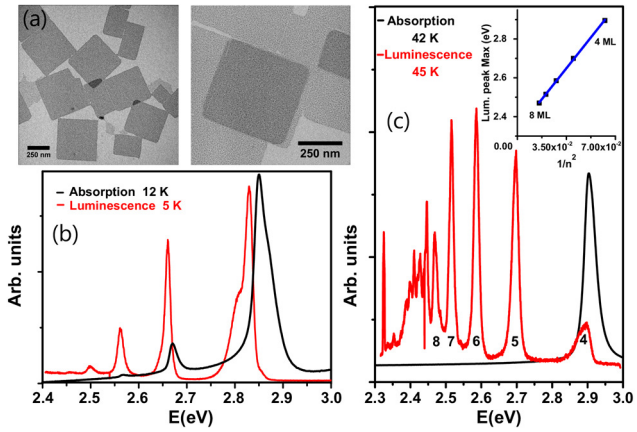

Figure 2: (a) TEM images of films synthetized following the procedure described in the text with addition of 240 µL HBr (samples B1). They contain large square NPLs with thicknesses identified here through their luminescence given in Figures (b) and (c). (b)-(c) Absorptions (black) and emissions (red) spectra obtained at two temperatures as close as possible (samples B2 and B3 respectively). Luminescence in (b) and (c) is measured after excitation at 400 nm and 395 nm respectively. In (c) the luminescence peaks of sample B3 are labeled with numbers *n* corresponding to the different thicknesses L_z of the NPLs ($L_z = n\,a$; a is the interplanar distance). Inset: Energies of the emission peaks shown in (c) and labeled by n as a function of $1/n^2$. From the linear fit to the data the interplanar distance a = 0.580 ± 0.005 nm is obtained.

Let us now focus onto the second class of nanostructures studied in this work *ie* NSTs. Sample A2 obtained from a synthesis of type A was characterized by TEM and optical absorption. Figure 3a, left panel, shows a typical TEM image whereas the right panel is a high-resolution TEM (HTEM) image of a single NST in which the detailed atomic structure appears. The thickness associated to a single octahedral layer can be extracted, $a \approx 0.58$ nm, in perfect agreement with the value deduced from the Equation (2)-based adjustment. As already observed in the aged sample (sample A1), two different – and classical - arrangements of NSTs with respect to the substrate are visible: some with face parallel to the substrate (appearing less dark in the image of Figure 3b) and others standing 'perpendicular' to the substrate (appearing darker in the image of Figure 3b). The measurement of the thickness is straightforward in those stacked edge-lying NSTs whereas an access to the lateral dimension is possible in the other ones. Lengths can be measured in any of the two populations. Figure 3c shows the length value distribution deduced from the analysis of TEM image (Fig. 3a, left side). An average of 40 nm is found. Additionaly, the analysis shows that, in average, the smaller lateral dimension is ≈ 4 to 5 nm and the thickness ≈ 3 nm. The corresponding histogram is provided in Figure 3d.

Because the two dimensions (thickness and width) are comparable to the exciton Bohr diameter, confinement effects have to be considered along two directions, *z* and *x* in NSTs. The absorption spectra at 12 K and 280 K of sample A2 are shown in Figure 4a (see also Figure S. 1a, SI). In particular, the low temperature spectrum presents many peaks in the high-energy range (≥ 2.7 eV). These numerous peaks cannot be attributed to the absorption of NPLs, in particular, the energy of the dominant ones (2.78, 2.83 and 3.02 eV) does not match results measured for the 5 and 4 MLs thick NPLs. Moreover, 1 (0.58 nm) - 3 MLs (1.74 nm) NPLs have not been observed in TEM images and would not explain the presence of the high-energy peaks. Comparable spectra with same resonant peaks but showing different intensities have been observed in other samples obtained with a similar synthesis procedure (sample A3, see ESI, Figure S. 2).

In NSTs, the ground and excited electronic states can be closer than in NPLs and the size dispersion in the thickness (L_z) and width (L_x) may lead to numerous absorption lines. The general expression for the optical transition energy of NSTs, when strong confinement and infinite wells are considered in the two directions *x* and *z*, is written:

$$E^{m_z,m_x} = E_g - E_b + m_z^2 \frac{\hbar^2\pi^2}{2\mu L_z^2} + m_x^2 \frac{\hbar^2\pi^2}{2\mu L_x^2} \qquad (3)$$

where L_x (L_z) is the confinement length in the *x* (*z*) direction ; m_x (m_z) is a quantification integer number along *x* (*z*) direction ($L_z < L_x$). The first optical transition corresponds to $m_z = 1$ and $m_x = 1$ and the second optical transition to $m_z = 1$ and $m_x = 2$. As deduced from the analysis of the NPL optical spectra, the size of the nanostructure is quantified by the lattice parameters. For NSTs it is necessary to know the orientation of the crystal with respect to the NSTs faces. In a recent

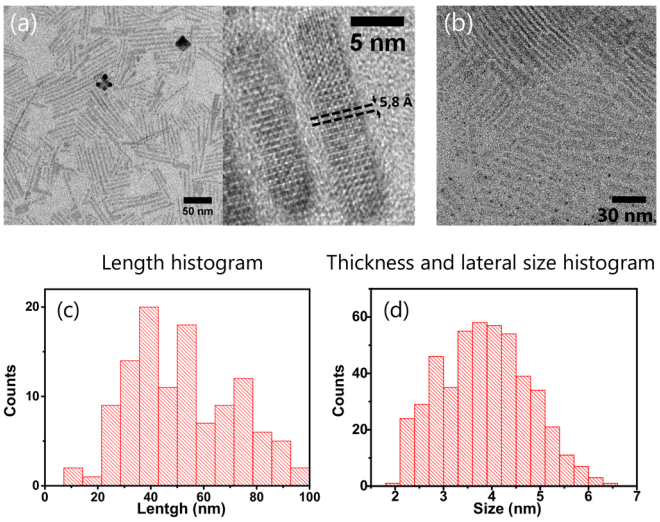

Figure 3: Structural analysis of $CsPbBr_3$ NPLs. (a) TEM images of $CsPbBr_3$ NPLs obtained in a class of syntheses explored in this work *ie* in hexane and without HBr (samples A2), leading to elongated objects, NSTs (left), whose crystal planes can be evidenced by HTEM images (right) on which the interplanar distance of 0.58 nm is measured. (b) Image of NPLs (sample A4, same synthesis as for (a)) where flat-lying (bottom of the image) and stacked edge-lying (top of the image) bars NPLs can be clearly observed. (c)-(d) Histograms of length and thickness/lateral size, respectively, corresponding to the typical image shown in (a) (left).

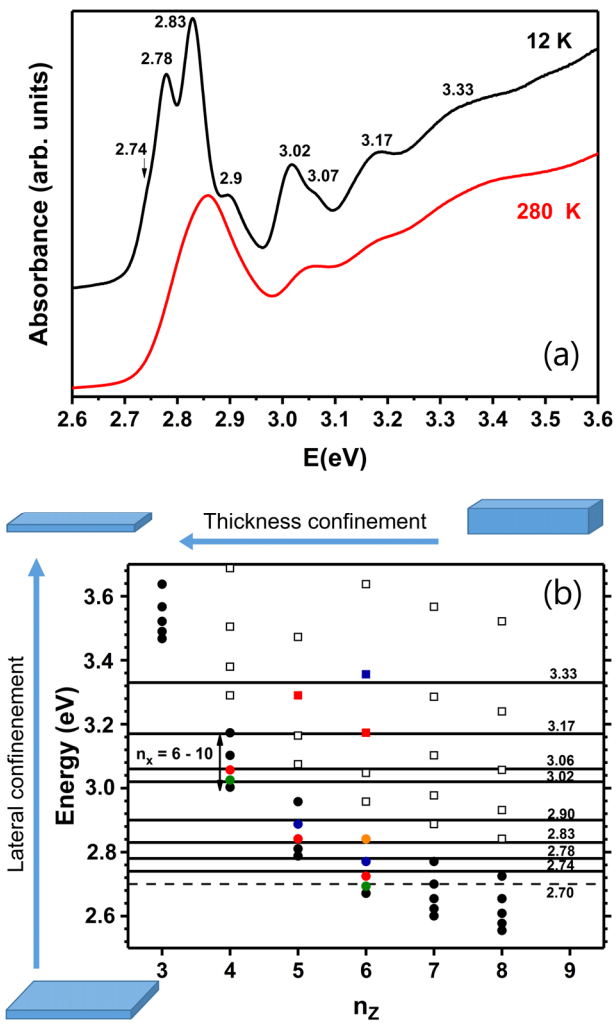

Figure 4: (a) Absorption spectra at 12 K and close to room temperature of dropcasted $CsPbBr_3$ NSTs film, sample A2, from synthesis A *ie* without HBr (see ESI, section I.). (b) First (full black circles) and second (open black squares) theoretical optical transitions vs n_z. The n_x values are in the 6 – 10 range. Experimental transitions (black lines). The dashed line is for the low energy transition observed in PL. Colorful symbols correspond to theoretical close to experimental lines. Each color is associate to one specific NST width n_x = 6 (orange), 7 (blue), 8 (red), 9 (green).

structural and morphological study of NPLs with thickness of 6 MLs and lateral size of about 10 nm,[29] authors found a specific orientation leading to an interplanar distance of 0.58 nm visible in all the faces. The HTEM images (Figure 3a, right) show an interplanar distance $a = 0.58$ nm in the two explored directions indicating, in agreement with the already cited reference, that in the perpendicular direction we will have the same interplanar distance (whatever cubic or orthorhombic crystal structure). We have then fixed the relations $L_z = n_z a$ and $L_x = n_x a$, with n_z and n_x integer numbers. This leads to the optical transition energies:

$$E_{n_z,n_x}^{m_z,m_x} = E_g - E_b + m_z^2 \frac{E_0}{n_z^2} + m_x^2 \frac{E_0}{n_x^2} \qquad (4)$$

with $E_0 = 9.56$ eV, as measured previously, and we set $E_g - E_b = 2.31$ eV.

Using Equation (4), we have represented in Figure 4b the first (full black circles) and the second (open black squares) optical transitions for different n_x values (6 – 10) and in the range $n_z = 3 - 8$. Horizontal solid lines represent the energies of the absorption peaks observed in the Figure 4a spectra. (n_x, n_z) values have been chosen to be in the length range observed by TEM, while reproducing the optical transition energies. In Figure 4b, the colorful symbols are associated to energies close to observed optical transitions. The intersection of horizontal lines and symbols give the NPL sizes associated to the observed optical transitions. At low energy, the optical transition at 2.74, 2.78 and 2.83 eV are related to the theoretical values $E_{6,8}^{1,1} = 2.73$ eV, $E_{6,7}^{1,1} = 2.77$ eV, $E_{5,9}^{1,1} = 2.81$ eV and $E_{5,8}^{1,1} = 2.84$ eV with a very good agreement. Moreover, the second optical transitions associated to these NSTs are equal to $E_{5,9}^{1,2} = 3.16$ eV, $E_{6,8}^{1,2} = 3.17$ eV, $E_{6,7}^{1,2} = 3.36$ eV and $E_{5,8}^{1,2} = 3.29$ eV ; once again, these values are coherent with the observed transitions at 3.17 eV and 3.33 eV, this last peak being very broad. Note that $E_{6,6}^{1,1} = 2.84$ eV could also explain the 2.83 eV transition, but the second transition $E_{6,6}^{1,2} = 3.64$ eV is too high to explain the 3.33 eV broad line. Finally, the absorption peaks observed at 2.90 eV, 3.02 eV and 3.06 eV are associate to smaller NSTs and can be well reproduced by the theoretical values $E_{5,7}^{1,1} = 2.89$ eV, $E_{4,9}^{1,1} = 3.03$ eV and $E_{4,8}^{1,1} = 3.06$ eV. In Figure 4b, we have also shown the main PL peak (dashed line) observed at 2.70 eV, and not visible on the absorption spectra because related to less numerous NSTs. This energy corresponds to the transition $E_{6,9}^{1,1} = 2.69$ eV.

It appears then possible to reproduce all the first and second optical transitions observed in a very structured absorption spectra, using a simple model, with previously measured parameters $(E_g - E_b,\ E_0)$, few (n_x, n_z) couples and a very small dispersion: (4, 8-9), (5, 7-9) and (6, 6-8). This analysis of the electronic levels and optical transitions is also reinforced by the typical NST sizes observed by TEM (see Figure 3a and histogram 3d), consistent with the theoretical size values $L_z = n_z a$ (2.32 – 3.48 nm) and $L_x = n_x a$ (3.48 – 5.22 nm).

From now, we will focus our study onto the properties of sample A2 containing NSTs. The low temperature PL spectrum excited at 370 nm is shown in Figure 5a. It can be adjusted using Gaussian profiles (see Figures S. 3 and S. 4 in the ESI). The transitions visible in the PL spectrum (three higher energy peaks) are present at the same energy in the absorption, and this is probably the reason why the PL at higher energy is strongly reabsorbed and not very intense. The PL spectrum also shows a peak at 2.70 eV, a shoulder at 2.73 eV and a smaller contribution at 2.78 eV. On the basis of the previous analysis we assume that all these structures may be associated to the presence of less represented NSTs with different sizes

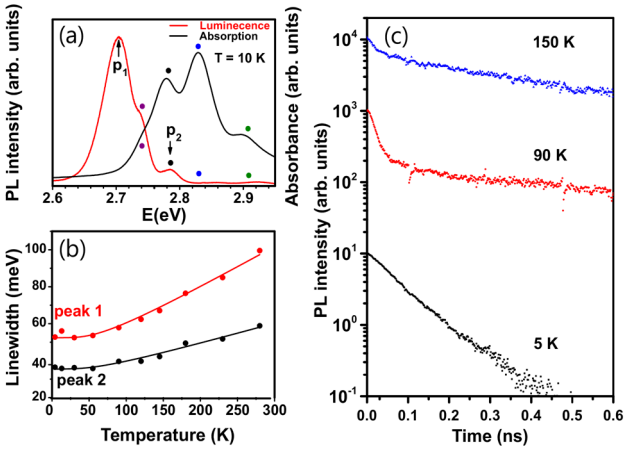

Figure 5: (a) Absorption (black) and emission (red) of a dropcasted $CsPbBr_3$ NSTs film, sample A2, at 10 K. The emission is obtained after excitation at 370 nm. Filled circles of a given color identify peaks or shoulders that share the same energy in the absorption and emission spectra and that likely correspond to the same transition: the energies considered here (2.74, 2.78, 2.83 and 2.90 eV) are those marked by the first four horizontal solid black lines in Figure 4 (b). (b) Temperature evolutions of the linewidths for the two most marked luminescence peaks: peaks 1 and 2, in (a). The linewidths are obtained though Gaussian adjustments of PL spectrum (see ESI, section II. Fig. S. 3). The lines are fits according to equation (5) obtained for $T_{phonon,LO}$ = 185 K (E_{LO}= 16 meV *ie* 130 cm^{-1}). (c) PL dynamics detected at 460 nm after excitation at 410 nm at 5, 90 and 150 K. The dynamics is faster at low temperatures, clearly bi-exponential at 90 K, and again almost exponential at higher temperatures where dynamics is slower. Solid lines are bi-exponential adjustments (characteristic times: 80 ps (single significant time measured) at 5 K; 18 and 290 ps at 90 K; ≈ 20 and 390 ps at 150 K).

(see Figure 4b). The study of the intensity of the low temperature PL peaks as a function of the density of excitation (see Figures S. 5 and S. 6 in ESI) shows that all peaks have the same linear behaviour supporting the hypothesis that we deal with different sizes of NSTs and not with different states in NSTs with the same size.

We have also studied the PL behaviour as a function of temperature. When the temperature is raised from 4 K to 280 K, we observe that all PL peaks slightly move to the blue as the bulk energy gap of the inorganic Cs-based perovskite materials (see Figures S. 1b, SI). Figure 5b shows the linewidth evolution, $\gamma(T)$, of the two more identifiable PL peaks (at 2.70 eV and 2.78 eV) as a function of the temperature. Assuming that the typical expression used in the bulk single crystal for linewidth of excitons is valid for nanocrystals,[51,55] $\gamma(T)$ is modelled as:

$$\gamma(T) = \gamma_0 + A_{ac}\,T + B_{LO}\,n_{LO}(T) \quad (5)$$

where γ_0 is an inhomogenous linewidth at null temperature. The second and third terms are broadening terms resulting from acoustic and LO phonons (Fröhlich) scattering with coupling constants A_a and B_{LO}, respectively. $n_{LO}(T)$ is the Bose-Einstein distribution function for the LO phonons and

$_{LO}$ is an average representative energy for the weakly dispersive LO phonon branch.[56,57] The coupling with acoustic phonons for perovskite materials is weak and we have considered it negligible as compared to the exciton-LO phonons coupling.[58] For the peak at 2.70 and 2.78 eV respectively, we obtain γ_0 = 53 meV and 36 meV, B_{LO} = 40 and 20 meV for $E_{LO} \approx$ 130 cm^{-1}. This average E_{LO} value is indeed found in bulk lead-bromine perovskites.[47,59] In average, we thus measure, in $CsPbBr_3$ NPLs, a stronger exciton–phonon coupling than in CdSe quantum dots (B_{LO} = 20 meV) and NPLs (B_{LO} = 11 meV).[53]

Finally, we comment about time-resolved luminescence experiments that have been carried out on NSTs for different temperatures. Dynamics of the emission at 2.69 eV (460 nm) are shown in Figure 5c for T = 5 K, 90 K and 150 K. At the lowest-temperature a short component of the order of 80 ps dominates in the decay, as was already observed in nanocrystals.[47] When the temperature is raised a longer component gains in intensity; it is typically visible above 50 K when using our Streak camera - with relatively poor intensity dynamical response - but we conjecture its presence may be revealed at lower temperature. Between 50 K and 150 K a rough analysis based on a bi-exponential model for the PL decay curves clearly indicates the simultaneous and monotonous decrease of both the short and long decay constants as T increases. We notice that above 150 K, the PL dynamics is mainly dominated by the long decay mechanism. As in nanocrystals of regular semiconductors and perovskite, this characteristic behaviour strongly suggests an influence played by a lower energy dark exciton on the bright exciton emission properties when the fine structure exciton states are thermally mixed and govern the luminescence dynamics.[60,61] Thorough studies on this particular point, as well as the estimation of the contribution to the relaxation of radiative/non-radiative channels, in all inorganic NPLs (and NSTs) will be the subject of future work.

Conclusions

The method of synthesis used in this work originally leads to nanocrystals showing confinement along two directions under the form of anisotropic nanosticks (NSTs). The additional introduction of HBr along the synthesis process leads to samples whose optical response may be perfectly characterized resorting to a unique confinement length and that we believe to be quasi-perfect nanoplatelets (NPLs). We further show that aging may have a similar effect on batches or films initially containing NSTs, promoting the formation of NPLs. The joint analyses of TEM images and spectroscopy data collected at low temperature allow us to determine the level of anisotropy in NSTs and to quantify the associated sizes. In particular confinement effects are evidenced in the two types of systems. In NPLs of thickness L_z, the transitions energies scales linearly as a function of L_z^{-2}, as expected in the strong confinement regime limit. A quasi perfect dependence is observed with decreasing L_z down to 4 MLs, providing insights

Please do not adjust margins

into the compensation mechanism between image charges effects and strengthening of the exciton binding in highly confined perovskite-based nanocrystals. We further show the drastic dependence of the optical response with respect to the precise morphology of NSTs. At low-temperature, inhomogeneous broadening is the main contribution to the absorption linewidth. In highly confined NPLs this inhomogeneous contribution definitely cannot result from the distribution in the NPLs thicknesses that would lead to huge displacements (≈ 100 meV). We believe that lateral size dispersion is the origin of this residual broadening, especially considering the small energy shifts of the exciton transition induced by the weak confinement operating in the lateral directions. On the one hand, NSTs and NPLs show very good luminescence properties and are fundamentally appropriate materials to study confinement and anisotropic shape effects on halide perovskites exciton properties, as lifetime, phonon coupling and fine structure. On the other hand, many specific and innovative properties make colloidal platelets and close derivatives, unique systems with advantages that are not shared by their epitaxial counterparts. Stick-shaped structures and platelets obtained through the colloidal route indeed remain bricks of utmost interest due to facile incorporation capabilities in organic materials allowing to combine functionalities in molecular electronic and optoelectronic devices for instance. Let us note that their excellent optoelectronic properties make 2D $CsPbBr_3$ systems very serious candidates for the next-generation high-performance photodetectors.[62] Moreover, the access to facile deposition methods paves the way to important developments in advanced nanophotonics or quantum optics using such nanocrystals as gain media, either in ensemble, as for instance in microcavity polaritonics[63], or as individual emitters coupled to nanoguides.[64] The control of self-assembling or post-orientation[65] might also provide an access to renewed or improved emission properties, like superfluorecence[66] but should also facilitate the penetration of new fields such as excitonic spin physics that requires well controlled magneto-optical configurations (free of orientation disorder) and that starts to be investigated in perovskite bulk-like materials.[67,68]

Authorship

E.L. synthesized the NCs and achieved with J.R structural characterization; V.S., J.R., L.L. performed the experimental work; M.B. and M.V. carried out the technical developments in cryogenics and the mechanical adaptation work of the cryostats used; I.S., A.G., K.B., C.T. and F.B. provided the theoretical support (ESI); V.S, J.R., T.B., C.T., L.L. and M. C. wrote the paper.

Conflicts of interest

There are no conflicts to declare.

Acknowledgements

This work was supported by French State funds managed by the ANR within the Investissements d'Avenir program under reference ANR-11-IDEX-0004-02, and more specifically within the framework of the Cluster of Excellence MATISSE and also by the ANR grants IPER-Nano2 (ANR-18CE30-0023-01), Copin (ANR-19-CE24-0022), Frontal (ANR-19-CE09-0017), Graskop (ANR-19-CE09-0026). VS, TB, LL, FB, MC and CT are grateful to Florent Margaillan for the invaluable support in optics at INSP. EL thanks the support ERC starting grant blackQD (Grant n° 756225). IS, AG and KB thank the financial support of Tunisian Ministry of Higher Education and Scientific Research.

Notes and references

1 W. Koh, A. C. Bartnik, F. W. Wise and C. B. Murray, *J. Am. Chem. Soc.*, 2010, **132**, 3909–3913.
2 S. Deka, K. Miszta, D. Dorfs, A. Genovese, G. Bertoni and L. Manna, *Nano Lett*. 2010, **10**, 3770–3776.
3 C. Schliehe, B. H. Juarez, M. Pelletier, S. Jander, D. Greshnykh, M. Nagel, A. Meyer, S. Foerster, A. Kornowski, C. Klinke and H. Weller, *Science*, 2010, **329**, 550–553.
4 G. B. Bhandari, K. Subedi, Y. He, Z. Jiang, M. Leopold, N. Reilly, H. P., Lu, A. TL. Zayak and L. Sun, *Chem. Mater.,* 2014, **26**, 5433–5436.
5 J. Joo, J. Sung Son, S.G. Kwon, J.H. Yu and T. Hyeon, *J. Am. Chem Soc.,* 2006, **128**, 5632–5633.
6 S. Ithurria and B. Dubertret, *J. Am. Chem. Soc*., 2008, **130**, 16504–16505.
7 S. Ithurria, M. D. Tessier, B. Mahler, R.P.S.M. Lobo, B. Dubertret and Al. L. Efros, *Nat. Mater.* 2011, **10**, 936–941.
8 B. Mahler, B. Nadal, C. Bouet, G. Patriarche and B. Dubertret, *J. Am. Chem. Soc*., 2012, **134**, 18591–18598.
9 M. Nasilowski, B. Mahler, E. Lhuillier, S. Ithurria and B. Dubertret, *Chem. Rev,* 2016, **116**, 10934–10982.
10 E. Lhuillier, S. Pedetti, S. Ithurria, B. Nadal, H. Heuclin and B. Dubertret, *Acc. Chem. Res*., 2015, **48**, 22–30.
11 M. D. Tessier, C. Javaux, I. Maksimovic, V. Loriette and B. Dubertret, *ACS Nano*, 2012, **6**, 6751–6758.
12 R. Scott, A. W. Achtstein, A. V. Prudnikau, A. Antanovich, L. D. A. Siebbeles, M. Artemyev and U. Woggon, *Nano Lett.,* 2016, **16**, 6576–6583.
13 A. Brumberg, S. M. Harvey, J. P. Philbin, B. T. Diroll, B. Lee, S. A. Crooker, M. R. Wasielewski, E. Rabani and R. D. Schaller, *ACS Nano*, 2019, **13**, 8589–8596.
14 A. Yeltik, S. Delikanli, M. Olutas, Y. Kelestemur, B. Guzelturk and H. V. Demir, *J. Phys. Chem. C*, 2015, **119**, 26768–26775.
15 B. Guzelturk, Y. Kelestemur, M. Olutas, S. Delikanli and H. V. Demir, *ACS Nano,* 2014, **8**, 6599–6605.
16 M. Olutas, B. Guzelturk, Y. Kelestemur, A, Yeltik, S. Delikanli and H. V. Demir, *ACS Nano*, 2015, **9**, 5041–5050.
17 M. Li, M. Zhi, H. Zhu, W. Wu, Q. Xu, M. H. Jhon and Y. Chan, *Nat. Commun.,* 2015, **6**, 8513–8521.
18 M. C. Weidman, M. Seitz, S. D. Stranks and W. A. Tisdale, *ACS Nano*, 2016, **10**, 7830–7839.
19 J. C. Blancon, A. V. Stier, H. Tsai, W. Nie, C. C. Stoumpos, B. Traoré, L. Pedesseau, M. Kepenekian, F. Katsutani, G. T. Noe, J. Kono, S. Tretiak, S. A. Crooker, C. Katan, M. G. Kanatzidis, J. J. Crochet, J. Even and A. D. Mohite, *Nat. Commun.,* 2018, **9**, 2254–2264.
20 S. T. Ha, X. Liu, Q. Zhang, D. Giovanni, T. C. Sum and Q. Xion, *Adv. Optical Mater.,* 2014, **2**, 838–844.
21 V. A. Hintermayr, A. F. Richter, F. Ehrat, M. Doblinger, W. Vanderlinden, J. A. Sichert, Y. Tong, L. Polavarapu, J. Feldmann and A. S. Urban, *Adv. Mater.,* 2016, **28**, 9478–9485.
22 O. Vybornyi, S. Yakunin and M. V. Kovalenko, *Nanoscale*, 2016, **8**, 6278–6283.

Please do not adjust margins

Please do not adjust margins

23 M. C. Weidman, A. J. Goodman and W. A. Tisdale, *Chem Mater*., 2017, **29**, 5019–5030.
24 M. B. Teunis, A. Jana, P. Dutta, M.A. Johnson, M. Mandal, B.B. Muhoberac and R. Sardar, *Chem. Mater*., 2016, **28**, 5043–5054.
25 Y. Bekenstein, B. A. Koscher, S. W. Eaton, P. Yang and A. P. Alivisatos, *J. Am. Chem. Soc.,* 2015, **137**, 16008–16011.
26 S. Sun, D. Yuan, Y. Xu, A. Wang and Z. Deng, *ACS Nano,* 2016, **10**, 3648–3657.
27 Q. A. Akkerman, S. Genaro Motti, A. R. S. Kandada, E. Mosconi, V. D'Innocenzo, G. Bertoni, S. Marras, B. A. Kamino, L. Miranda, F. De Angelis, A. Petrozza, M. Prato and L. Manna, *J. Am. Chem. Soc.*, 2016, **138**, 1010–1016.
28 J. Cho, H. Jin, D.G. Sellers, D. F. Watson, D. H. Son and S. Banerjee, *J. of Materials Chemistry C*. 2017, **5**, 8810–8818.
29 F. Bertolotti, G. Nedelcu, A. Vivani, A. Cervellino, N. Masciocchi, A. Guagliardi and M. V. Kovalenko, *ACS Nano,* 2019*,* **13**, 14294–14307.
30 J. B. Bohn, Y. Tong, M. Gramlich, M. L. Lai, M. Doblinger, K. Wanf, R. L. Z. Hoye, P. Müller-Buschbaum, S. D. Stranks, A. S. Urban, L. Polavarapu and J. Feldmann, *Nano Lett*. 2018, **18**, 5231–5238.
31 C. Huo, Ch.F. Fong, M.-R. Amara, Y. Juang, B. Chen, J. Zhang, L. Guo, H. Li, W. Juang, C. Diederichs and Q. Xiong, *Nano Lett.*, 2020, **20**, 3673–3680.
32 D. Zhang, S. W. Eaton, Y. Yu, L. Dou and P. Yang, *J. Am. Chem. Soc.*, 2015, **137**, 9230–9233.
33 M. Imran, F. Di Stasio, Z. Dang, C. Canale, A.H. Khan, J. Shamsi, R. Brescia, M. Prato and L. Manna, *Chem. Mater.*, 2016, **28**, 6450–6454.
34 Y. Tong, M. Fu, E. Bladt, H. Huang, A. F. Richter, K. Wang, P. Müller-Buschbaum, S. Bals, P. Tamarat, B. Lounis, J. Feldmann and L Polavarapu, *Angew. Chem.,* 2018, **130**, 16326–16330.
35 H. Zhu, Y. Fu, F. Meng, X. Wu, Z. Gong, Q. Ding, M. V. Gustafsson, M. T. Trinh, S. Jin and X. Y. Zhu, *Nat. Mater.,* 2015, **14**, 636–642.
36 S. W. Eaton, L. Minliang, N.A. Gibson, A. B. Wong, L. Dou, J. Ma, L.-W. Wang, S. R. Leone, and P. Yang, *Proceeding of the National Academy of Sciences of the United States of Am.*, 2016, **113**, 1993–1998.
37 Q. Zhang, S. T. Ha, X. Liu, T. C. Sum and Q. Xiong, *Nano Lett.,* 2014, **14**, 5995–6001.
38 Y. Ling Y, Z. Yuan, Y. Tian, X. Wang, J. C. Wang, Y. Xin, K. Hanson, B. Ma and H. Gao, *Adv. Mater.,* 2016, **28**, 305–311.
39 F. Yan, S. T. Tian, X. Li and H. V. Demir, *Small,* 2019, **15**, 1902079.
40 Y. J. Zhao, Y. Qiu, H. Gao, J. Feng, G. Chen, L. Jiang and Y. Wu, *Adv. Mater.,* 2020, **32**, 1905298.
41 W. J. Mir, C. Livache, N. Goubet, B. Martinez, A. Jagtap, A. Chu, N. Coutard, H. Cruguel, T. Barisien, S. Ithurria, A. Nag, B. Dubertret, A. Ouerghi, M.G. Silly and E. Lhuillier, *Appl. Phys. Lett.,* 2017, **112**, 113503.
42 J. Song, L. Xu, J. Li, J. Xue, Y. Dong, X. Li and H. Zeng, *Adv. Mater.,* 2016, **28**, 4861–4869.
43 H. Huang, M. Liu, J. Li, L. Luo, J. Zhao, Z. Luo, X. Wang, Z. Ye, H. He and J. Zeng, *Nanoscale*, 2017, **9**, 104–108.
44 J. Ramade, L. M. Andriambariarijaona, V. Steinmetz, N. Goubet, L. Legrand, T. Barisien, F. Bernardot, C. Testelin, E. Lhuillier, A. Bramati and M. Chamarro, *Appl. Phys. Lett.,* 2018, **112**, 072104.
45 R. Ben Aich, I. Saidi, S. Ben Radhia, K. Boujdaria, T. Barisien, L. Legrand, F. Bernardot, M. Chamarro and C. Testelin. *Phys. Rev. Appl*., 2019, **11**, 034042.
46 R. Ben Aich, S. Ben Radhia, K. Boujdaria, M. Chamarro and C. Testelin, *J. Phys. Chem. Lett.*, 2020, **11**, 808–817.
47 J. Ramade, L. M. Andriambariarijaona, V. Steinmetz, N. Goubet, L. Legrand, T. Barisien, F. Bernardot, C. Testelin, E. Lhuillier, A. Bramati and M. Chamarro, *Nanoscale*, 2018, **10**, 6393–6401.
48 D. Sapori, M. Kepenekian, L. Pedesseau, C. Katan and J. Even, *Nanoscale*, 2016, **8**, 6369–6378.
49 G. Bastard, E. E. Mendez, L. L. Chang and L. Esaki, *Phys. Rev. B,* 1982, **26**, 1974–1979.
50 G. Garcia-Arellano, F. Bernardot, G. Karczewski, C. Testelin and M. Chamarro, *Phys. Rev. B*, 2019, **99**, 235301.
51 M.D. Lechner, *Refractive Indices of Organic Liquids*, Group III, vol 38B, Springer Berlin, 1996.
52 J. A. Sichert, Y. Tong, N. Mutz, M. Vollmer, S. Fisher, K. Z. Milowska, R. Garcia Cortadella, B. Nickel, C. Cardenas-Daw, J. K. Stolarczyk, A. S. Urban and J. Feldmann, *Nano Lett.*, 2015, **15**, 6521–6527.
53 A. W. Achtstein, A. Schliwa, A. Prudnikau, M. Hardzei, M. V Artemyev, C.Thomsen and U. Woggon, *Nano Lett.*, 2012, **12**, 3151–3157.
54 R. Benchamekh, N. A. Gippius, J. Even, M. O. Nestoklon, J. M. Jancu, S. Ithurria, B. Dubertret, Al. L. Efros and P. Voisin, *Phys. Rev B,* 2014, **89**, 035307.
55 T. Itoh and M. Furumiya, *J. Lumin.,* 1991, **48–49**, 704–708.
56 P. Y. Yu, M. Cardona, *Fundamentals of semiconductors physics and materials properties*; Springer: Berlin, 2003**.**
57 X. B. Zhang, T. Taliercio, S. Kolliakos and P. Lefebvre, *J. Phys. Condens. Matter.*, 2001, **13**, 7053–7074.
58 H. Long, X. Peng, J. Lu, K. Lin, L. Xie, B. Zhang, L. Ying and Z. Wei, *Nanoscale*, 2019, **11**, 21867–21871.
59 A. D. Wright, C. Verdi, R. L. Milot, G. E. Eperon, M. A. Pérez-Osorio, H. J. Snaith, F. Giustino, M. B. Johnston, and L. M. Herz, *Nat. Commun.*, 2016, **7**, 11755.
60 O. Labeau, P. Tamarat and B. Lounis, *Phys. Rev. Letters*, 2003, **90**, 257404.
61 L. Biadala, F. Liu, M. D. Tessier, D. R. Yakovlev, B. Dubertret and M. Bayer, *Nano Lett*., 2014, **14**, 1134–1139.
62 T. Yang, F. Li and R. Zheng, *ACS Applied Electronic Materials*, 2019, **1**, 1348–1366.
63 R. Su, S. Ghosh, J. Wang, S. Liu, C. Diederichs, T. C. H. Liew and Q. Xiong, *Nat. Phys.*, 2020, **16**, 301–306.
64 S. Pierini, M. D'Amato, M. Goyal, Q. Glorieux, E. Giacobino, E. Lhuillier, C. Couteau and A. Bramati, *ACS Photonics*, 2020, **7**, 2265–2272.
65 Y. Gao, M. C. Weidman and W. A. Tisdale, *Nano Lett*., 2017, **17**, 3837–3843.
66 G. Rainò, M. A. Becker, M. I. Bodnarchuk, R. F. Mahrt, M. V. Kovalenko and T. Stöferle, *Nature*, 2018, **563**, 671–675.
67 V. V. Belykh, D. R. Yakovlev, M. M. Glazov, P. S. Grigoryev, M. Hussain, J. Rautert, D. N. Dirin, M. V. Kovalenko and M. Bayer, *Nat. Commun*., 2019, **10**, 673.
68 D. Giovanni, H. Ma, J. Chua, M. Grätzel, R. Ramesh, S. Mhaisalkar, N. Mathews and T. C. Sum, *Nano Lett*., 2015, **15**, 1553–1558.

Please do not adjust margins